Appl. Math. Mech. -Engl. Ed., **44**(5), 693–710 (2023)

APPLIED MATHEMATICS AND MECHANICS (ENGLISH EDITION)

https://doi.org/10.1007/s10483-023-3001-6

A modified single edge V-notched beam method for evaluating surface fracture toughness of thermal barrier coatings*

Haoran BAI, Zhanyu WANG, Sangyu LUO, Zhaoliang QU†, Daining FANG

Institute of Advanced Structure Technology, Beijing Institute of Technology, Beijing 100081, China

(Received Mar. 23, 2023 / Revised Apr. 4, 2023)

Abstract The surface fracture toughness is an important mechanical parameter for studying the failure behavior of air plasma sprayed (APS) thermal barrier coatings (TBCs). As APS TBCs are typical multilayer porous ceramic materials, the direct applications of the traditional single edge notched beam (SENB) method that ignores those typical structural characters may cause errors. To measure the surface fracture toughness more accurately, the effects of multilayer and porous characters on the fracture toughness of APS TBCs should be considered. In this paper, a modified single edge V-notched beam (MSEVNB) method with typical structural characters is developed. According to the finite element analysis (FEA), the geometry factor of the multilayer structure is recalculated. Owing to the narrower V-notches, a more accurate critical fracture stress is obtained. Based on the Griffith energy balance, the reduction of the crack surface caused by micro-defects is corrected. The MSEVNB method can measure the surface fracture toughness more accurately than the SENB method.

Key words thermal barrier coating (TBC), surface fracture toughness, modified single edge V-notched beam (MSEVNB) method, multilayer structure, micro-defect

Chinese Library Classification O341, O346.1
2010 Mathematics Subject Classification 74B05, 74R10

1 Introduction

Air plasma sprayed (APS) thermal barrier coatings (TBCs) are widely used in gas turbine engines to protect hot-end components due to their excellent thermal insulation and corrosion resistance[1]. Generally, APS TBCs are multilayer coatings, which consist of a ceramic top coat, a metallic bond coat, and a metallic substrate[2]. The mismatch of the mechanical and thermal properties of different layers can result in stresses in APS TBCs. The stresses could

* Citation: BAI, H. R., WANG, Z. Y., LUO, S. Y., QU, Z. L., and FANG, D. N. A modified single edge V-notched beam method for evaluating surface fracture toughness of thermal barrier coatings. *Applied Mathematics and Mechanics* (*English Edition*), **44**(5), 693–710 (2023) https://doi.org/10.1007/s10483-023-3001-6

† Corresponding author, E-mail: quzl@bit.edu.cn

Project supported by the National Natural Science Foundation of China (Nos. 12172048 and 12027901) and the National Science and Technology Major Project of China (Nos. 2019-VII-0007-0147 and 2017-VI-0020-0093)

induce surface cracks in the top coats during service[3–7]. Surface cracks provide channels for external oxygen transport. It has been observed that oxygen has the ability to swiftly permeate the interface between the top coat and the bond coat via channels. This process can expedite the oxidation of the bond coat, which can ultimately result in the failure of TBCs[8–12]. Thus, studies on the failure induced by surface cracks should receive attention[13–15]. In particular, models describing and predicting the surface fracture behavior are urgently needed. To exactly describe and predict the surface fracture behavior, the surface fracture toughness, as an important parameter for model building, should be accurately determined[16].

Based on the linear elastic fracture mechanics (LEFM) theory, many experimental methods have been developed to evaluate the surface fracture toughness of APS TBCs[17], e.g., the dog-bone-shaped specimen tension method[18–20], the unnotched beam bending method[21–26], the indention fracture method[27–28], the micro-cantilever bending method[29], the double cantilever beam (DCB) bending method[30–31], and the single edge notched beam (SENB) bending method[25,32–33]. On account of adopting unnotched specimens, the dog-bone-shaped specimen tension method and unnotched beam bending method are not an optimal choice for measuring the surface fracture toughness based on the Griffith energy balance[17,34]. The indention fracture method is a typical semi-analytical empirical method, and needs further development[35–37]. Due to the large plastic zone in relation to the micrometer sample size, LEFM is inapplicable in the micro-cantilever bending method[38]. The DCB bending method is acceptable in terms of fracture mechanics, but the specimen preparation is more difficult and expensive[39]. Owing to its ease of operation and high stability, the SENB method is more commonly used[25,32–33].

In the case of blunt machined notches, the SENB method will overestimate the fracture toughness[39–40]. Thus, the single edge V-notched beam (SEVNB) bending method is developed, which is suitable for fracture toughness evaluations because of the narrower notches[39–40]. In the SEVNB method, the following equation is usually used to calculate the fracture toughness:

$$K_{\mathrm{Ic}} = f\sigma_{\mathrm{c}}\sqrt{\pi a}, \tag{1}$$

where K_{Ic} is the critical stress intensity factor of Mode I, f is a dimensionless geometry factor that depends on the specimen configuration, σ_{c} is the critical fracture stress, and a is the initial depth of the V-notch. The SEVNB specimens could obtain more accurate critical fracture stress than the SENB specimens because of the narrower notches[41]. The SEVNB method is originally designed for dense bulk materials, and is mainly used in advanced ceramics[39]. However, since APS TBCs are typical multilayer and porous materials, applying the SEVNB method directly to APS TBCs may cause errors. Hence, typical structural characters in TBCs should be considered during the tests. Considering the multilayer structure of APS TBCs and different properties of each layer, the dimensionless geometry factor f should be recalculated and determined. Besides, there are various micro-defects, including micro-cracks and micropores, in the top coat to achieve good thermal insulation[2], and the presence of micro-defects can reduce the area of crack surface and lead to underestimated fracture toughness according to the Griffith energy balance. Thus, those factors should be considered during the evaluation of surface fracture toughness for APS TBCs.

In this paper, a modified single edge V-notched beam (MSEVNB) method is applied and the effects of typical structural characters are considered to accurately measure the surface fracture toughness of APS TBCs. The results measured by the MSEVNB method are more accurate than those measured by the traditional SENB method.

2 Materials and methods

2.1 Materials and specimens

In this study, 8% (mole fraction) yttria stabilized zirconia (8YSZ) TBCs provided by United Coatings Technology Co., Ltd. (Beijing, China), were selected and characterized. The APS TBCs consist of a nickel-based superalloy substrate (GH3030), a metallic bond coat (NiC-

oCrAlY), and a ceramic top coats (8YSZ). To improve the interfacial adhesion between the bond coats and substrates, the substrate surface was sandblasted. Then, NiCoCrAlY powders were sprayed onto the substrates by the APS technique, and the average thickness of the bond coats was 100 μm. Finally, top coats with different thicknesses, including 400 μm, 600 μm, and 900 μm, were prepared. After spraying, the TBCs were cut into beam specimens with the dimensions of 20 mm × 2 mm × 3 mm (length×width×height), 20 mm × 2 mm × 2.7 mm, and 20 mm × 2 mm × 2.5 mm, as shown in Fig. 1(a). Some specimens were classified as the basic group, which was used to measure the elastic modulus, residual stress, and ultimate strength.

To measure the surface fracture toughness of TBCs, notches were introduced into the beam specimens with the dimensions of 20 mm × 2 mm × 3 mm by a diamond cutter. A through-width notch at the midpoint of the length direction was introduced into the top coat, and the notch depth was (450 ± 20) μm. In order to study the difference between the MSEVNB method and the SENB method, two types of specimens were produced. Depending on Gogotsi et al.[41], the MSEVNB specimens were machined by the diamond cutter with V-notches, and the notch root radius R was 10 μm. According to Ref. [33], the SENB specimens had straight-through notches, and the notch root radius R was 50 μm. The MSEVNB specimens were classified as the experimental group, while the SENB specimens were classified as the control group, as shown in Fig. 1(b).

To verify the accuracy of the MSEVNB method, the freestanding MSEVNB specimens with the dimensions of 20 mm × 0.9 mm × 2 mm were obtained by dissolving the substrates and bond coats of the beam specimens. Notches with the depth of 900 μm and the root radius of 10 μm were introduced. Those freestanding specimens were classified as the verification group-1, as shown in Fig. 1(c).

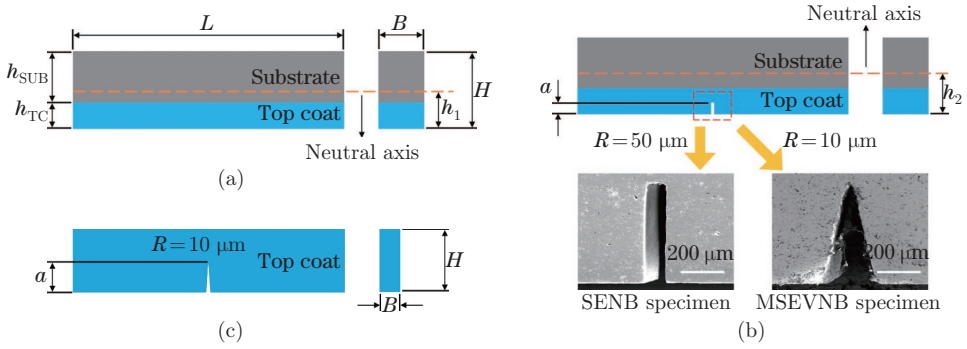

Fig. 1 Schematic of (a) beam specimens, (b) SENB and MSEVNB specimens, and (c) freestanding MSEVNB specimens (color online)

To verify the independence of the top coat thickness h_{TC} on the surface fracture toughness measured by the MSEVNB method, the notches with the depth of (300±20) μm were introduced into the beam specimens with the dimensions of 20 mm × 2 mm × 2.7 mm, and those with the depth of (200 ± 20) μm were introduced into the beam specimens with the dimensions of 20 mm × 2 mm × 2.5 mm. The notch root radius R was set as 10 μm. These two types of MSEVNB specimens were classified as the verification group-2 and the verification group-3, respectively.

The classifications and dimensions of all the specimens are listed in Table 1, where L, B, and H are the length, width, and height of the beam specimens, respectively, h_{TC} is the top coat thickness, a is the notch depth, and N is the number of the specimens per group.

2.2 In-situ three-point bending (3PB) tests

In-situ 3PB tests were performed by an in-situ scanning electron microscope (in-situ SEM), as shown in Fig. 2. The specimens were loaded by a mini in-situ mechanical testing system

Table 1 Classifications and dimensions of all the specimens

Group	L/mm	B/mm	H/mm	h_{TC}/mm	a/μm	R/μm	N
Basic group	20.0	2.0	3.0/2.7/2.5	0.9/0.6/0.4	–	–	7/7/7
Experimental group	20.0	2.0	3.0	0.9	450	10	10
Control group	20.0	2.0	3.0	0.9	450	50	10
Verification group-1	20.0	0.9	2.0	2.0	900	10	10
Verification group-2	20.0	2.0	2.7	0.6	300	10	10
Verification group-3	20.0	2.0	2.5	0.4	200	10	10

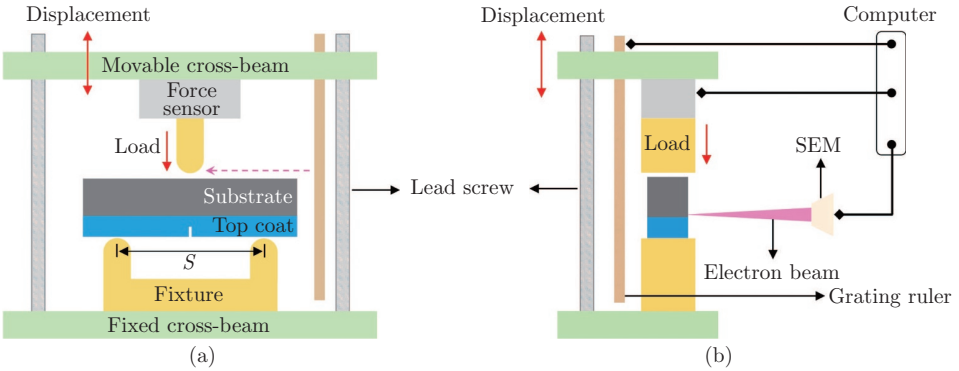

Fig. 2 Schematic of the in-situ 3PB device in (a) top view and (b) side view (color online)

(Qiyue, MINI-MTS) integrated with an SEM (Zeiss, Sigma 300). Loads were measured by a load sensor with 1 000 N range and 0.5 N resolution. Displacements were measured by a grating ruler with 10 mm range and 0.2 μm resolution. Both sensors were calibrated by a standard sample before the tests. Sigma 300 has a secondary electron imaging resolution of 10 nm, and can observe the crack tip clearly. Specimens were first placed on a specialized 3PB fixture with a span width of 16 mm. Before the in-situ 3PB tests, the micromorphology around the notch root was observed by the SEM. Then, a 0.5 μm/s displacement rate was used to load the specimens. To obtain the initiation and propagation process of crack near the notch root, the loading process paused for SEM imaging when the indenter moved every 1 μm. The load-displacement curves were obtained from the data recorded by the load sensor and grating ruler. Meanwhile, the micrographs of crack initiation and propagation process were also obtained. To measure the critical fracture stress σ_c and the ultimate strength σ_b, the critical loads were accurately determined according to the micrographs and load-displacement curves. The data collected were corrected for the instrument compliance.

2.3 X-ray diffraction (XRD) measurements of residual stress

It is well-known that there is residual stress in APS TBCs due to thermal mismatch[42]. The residual stress may lead to overestimation or underestimation of the critical fracture toughness σ_c and ultimate strength σ_b. To accurately determine σ_c and σ_b, the residual stress parallel to the surface direction σ_{res} should be measured[33,42]. XRD, as a fast and reliable non-destructive testing technology, has no specific requirements on specimen size and shape, and is suitable for the measurement of micro-area stress. It has been widely used to measure residual stress in TBCs. In this study, σ_{res} was determined by an X-ray stress analyzer (Stresstech Oy, XSTRESS 3000) according to Teixeira et al.[43], and beam specimens were used.

2.4 X-ray computed tomography (X-CT) measurements of porosity

The top coat prepared by the APS technique has a typical porous structure, which may affect the measurement of the fracture area and lead to errors in the measurement of fracture

toughness[44]. The micro-defects in the top coat should be quantitatively characterized. X-CT is a non-destructive testing technology for studying the internal structure. A freestanding top coat was polished to the size of 0.5 mm × 0.5 mm × 2 mm and measured by a submicron X-ray microscopy (Zeiss, Xradia 520 Versa). The spatial resolution was set as 800 nm. The data gathered by X-CT were processed by Avizo 2019. The micro-defects in the top coats were visualized, and the porosity was statistically calculated.

3 Results and discussion

3.1 Property measurement of APS TBCs

3.1.1 Elastic moduli of top coat and substrate

The elastic moduli of the top coat and substrate are important parameters, and should be accurately evaluated in the measurement of fracture toughness. Commonly, bond coat is regarded as one part of substrate, because it is much smaller than substrate in thickness and has similar mechanical properties[1]. The TBC specimens were simplified as a double-layer composite beam. Based on the Euler beam theory[45], the elastic modulus of substrate E_{SUB} can be calculated from the slope of linear section in the load-displacement curve according to

$$E_{\mathrm{SUB}} = \frac{S^3}{4Bh_{\mathrm{SUB}}^3}\frac{\Delta P}{\Delta \delta}, \tag{2}$$

where S is the span of the 3PB fixture, B is the width of specimens, h_{SUB} is the thickness of the substrate, P is the load, and δ is the displacement. $\Delta P/\Delta\delta$ is the slope of linear section in the load-displacement curve. A typical load-displacement curve during the 3PB tests on substrate is shown in Fig. 3(a). The value of E_{SUB} is determined as (167.92 ± 5.21) GPa.

According to the composite beam theory[46], the elastic modulus of the top coat E_{TC} can be written as

$$E_{\mathrm{TC}} = \frac{\frac{S^3}{16B}\frac{\Delta P}{\Delta \delta} - E_{\mathrm{SUB}}((h_1 - h_{\mathrm{TC}})^3 + (H - h_1)^3)}{h_1^3 - (h_1 - h_{\mathrm{TC}})^3}, \tag{3}$$

where δP is the slope of linear section in the load-displacement curve obtained from the 3PB tests on beam specimens, h_{TC} is the thickness of the top coat, and H is the height of the specimens. h_1 is the distance from the neutral axis to the surface of the top coat, and[46]

$$h_1 = \frac{E_{\mathrm{SUB}}h_{\mathrm{SUB}}^2 - E_{\mathrm{TC}}h_{\mathrm{TC}}^2}{2E_{\mathrm{SUB}}h_{\mathrm{SUB}} + 2E_{\mathrm{TC}}h_{\mathrm{TC}}} + h_{\mathrm{TC}}. \tag{4}$$

A typical load-displacement curve during the 3PB tests on beam specimens is shown in Fig. 3(b). Combining Eqs. (3) and (4), the value of E_{TC} is determined as (29.31 ± 2.08) GPa.

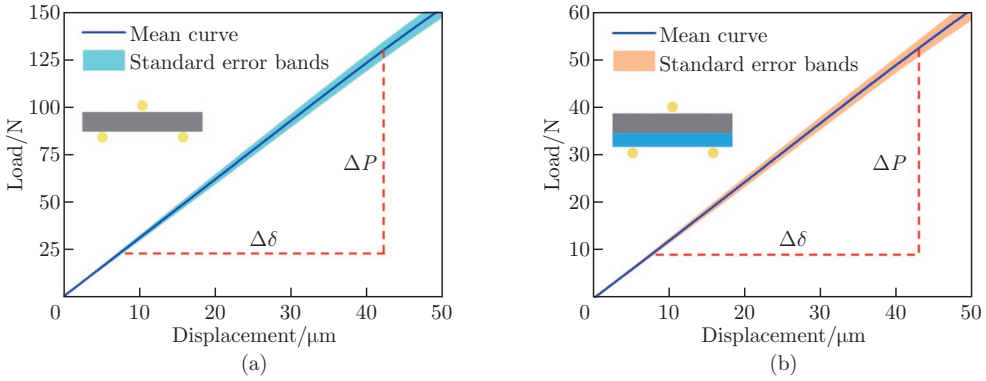

Fig. 3 Typical load-displacement curves during the 3PB tests on (a) substrate and (b) beam specimens (color online)

3.1.2 Residual stress in top coat

The residual stress near the crack tip should be considered when determining the critical fracture stress[33]. Then, the residual stress $\sigma_{\mathrm{res}}^{\mathrm{root}}$ parallel to the interface direction near the notch root in the top coat was measured. Due to the penetration ability of X-rays, the XRD method can only measure the sub-surface residual stress $\sigma_{\mathrm{res}}^{\mathrm{top}}$. To determine the residual stress near the notch root $\sigma_{\mathrm{res}}^{\mathrm{root}}$, XRD combined with layer stripping along the height of the top coat was applied[47]. Take the beam specimen with the height of 0.9 mm as an example. The residual stress along the thickness of the top coat is plotted in Fig. 4. It is found that tensile stress exists within the top coat, and decreases with the increasing grinding thickness. The residual stress near the notch root $\sigma_{\mathrm{res}}^{\mathrm{root}}$ is determined as (4.0 ± 2.2) MPa.

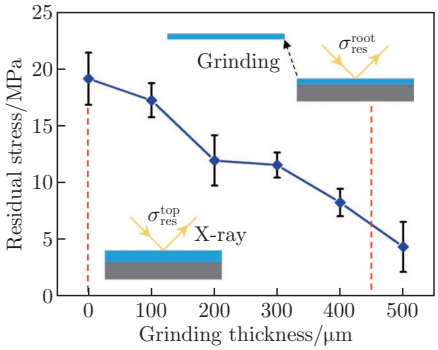

Fig. 4 Residual stress along the top coat thickness ($h_{\mathrm{TC}} = 0.9$ mm) (color online)

3.2 Surface fracture toughness of APS TBCs measured by MSEVNB method

To demonstrate the MSEVNB method in detail and show the difference between the SENB method and the MSEVNB method, the specimens in the experimental and control groups are chosen in this section.

3.2.1 Geometry factor influenced by multilayer structure

The geometry factor f of the bulk material can be expressed in two forms. These two forms can be mutually converted, and the trends are opposite with the increase in a/H. In this paper, the form of geometry factor corresponding to the critical fracture stress is chosen (a detailed interpretation of the geometry factor f is given in Appendix A). For example, Fett[48] has given the following equation of bulk material with $S/H = 16/3$:

$$f(x) = 1.123 - 3.40x + 7.00x^2 - 8.90x^3 + 5.12x^4, \tag{5}$$

where $x = a/H$. In Refs. [25] and [33], the dimensionless geometry factor f of the bulk material was directly used to evaluate the fracture toughness of the TBCs, where the multilayer structure of the TBCs was ignored. Different from bulk materials, TBCs are typical multilayer materials with different elastic properties. To obtain a more accurate geometry factor f^*, the multilayer structure of TBCs should be considered.

The geometry factor can be determined by the finite element analysis (FEA) with the J-integral method[38]. On the basis of the LEFM, the fracture toughness can be expressed as

$$K_{\mathrm{Ic}} = \sqrt{\frac{J_{\mathrm{Ic}} E_{\mathrm{TC}}}{1 - v_{\mathrm{TC}}^2}}. \tag{6}$$

Combining Eqs. (1) and (6) yields

$$f = \frac{1}{\sigma_{\mathrm{c}}} \sqrt{\frac{J_{\mathrm{Ic}} E_{\mathrm{TC}}}{\pi a (1 - v_{\mathrm{TC}}^2)}}, \tag{7}$$

where J_{Ic} is the critical contour integral, and can be calculated by the FEA, which will be discussed in the next paragraph in detail. E_{TC}, v_{TC}, and a are given values in the FEA model. σ_{c} is the critical fracture stress, and can be determined by (a detailed derivation of σ_{c} is given in Appendix B)

$$\sigma_{\mathrm{c}} = \frac{12E_{\mathrm{TC}}P_{\mathrm{c}}S(h_2 - a)}{E_{\mathrm{SUB}}B((h_2 - h_{\mathrm{TC}})^3 - (h_2 - H)^3) + E_{\mathrm{TC}}B((h_2 - a)^3 - (h_2 - h_{\mathrm{TC}})^3)}, \tag{8}$$

where P_{c} is the critical load when crack emerges at the notch root. h_2 is the distance from the neutral axis to the surface of the top coat in notched specimens. Similar to the derivation of h_1 in Eq. (4), h_2 is expressed as

$$h_2 = \frac{E_{\mathrm{SUB}}h_{\mathrm{SUB}}^2 - E_{\mathrm{TC}}(h_{\mathrm{TC}} - a)^2}{2E_{\mathrm{SUB}}h_{\mathrm{SUB}} + 2E_{\mathrm{TC}}(h_{\mathrm{TC}} - a)} + h_{\mathrm{TC}}. \tag{9}$$

Based on the FEA results and Eqs. (7)–(9), the geometry factor can be obtained. In this study, collapse elements are used to simulate the singularity of crack tip in the FEA[48–49]. Two-dimensional (2D) FEA models with different values of x are established in ABAQUS 2020. The materials are set to be pure elastic and isotropic. The elastic modulus and Poisson's ratio of the substrate are set as 167.92 GPa and 0.285[1], respectively. The elastic modulus and Poisson's ratio of the top coat are set as 29.31 GPa and 0.21[1], respectively. The notch is set as one seam, and the elements around the crack tip are divided into the spiderweb including 5 contours. To simulate the $1/\sqrt{r}$ strain singularity of the crack tip based on the LEFM, the nodes at the crack tip are normally tied, and the mid-side nodes are moved to the 1/4 points, as shown in Fig. 5(a). 6-node quadratic plane strain triangle elements (CPE6) are used to discretize the crack tip, while 8-node biquadratic plane strain quadrilateral elements (CPE8) are used for other elements[38]. The displacement rate control mode is adopted, and the displacement rate is set as 0.5 μm/s. The model geometry and stress distribution around the crack tip are presented in Fig. 5(b). The results of contour integral at different a/H are also plotted in Fig. 5(c).

To verify the accuracy of the FEA results, the shape factor of the bulk materials with $S/H = 16/3$ is calculated and expressed as

$$f^{\#}(x) = 1.089 - 3.71x + 11.23x^2 - 25.53x^3 + 27.43x^4. \tag{10}$$

Compared with f given by Fett[48], $f^{\#}$ is close to it. It demonstrates that the geometry factor calculated by the FEA is effective. The geometry factor considering the multilayer structure of TBCs f^* is plotted in Fig. 5(d), and is expressed as

$$f^*(x) = 1.055 - 2.74x + 11.76x^2 - 36.59x^3 + 38.98x^4. \tag{11}$$

It is found that f is about 11% lower than f^* when $x = 0.15$ and a =450 μm. According to Eq. (1), if the geometry factor of the bulk material is directly used in TBCs, the fracture toughness would be underestimated by 11%.

3.2.2 Critical fracture stress influenced by notch root radius

When crack emerges at the notch root, after taking the residual stress into consideration, the critical fracture stress σ_{c} is determined by

$$\sigma_{\mathrm{c}} = \frac{12E_{\mathrm{TC}}P_{\mathrm{c}}S(h_2 - a)}{E_{\mathrm{SUB}}B((h_2 - h_{\mathrm{TC}})^3 - (h_2 - H)^3) + E_{\mathrm{TC}}B((h_2 - a)^3 - (h_2 - h_{\mathrm{TC}})^3)} + \sigma_{\mathrm{res}}^{\mathrm{root}}. \tag{12}$$

After measuring the residual stress, in-situ 3PB tests are carried out to determine the critical fracture stresses σ_{c} of the MSEVNB and SENB specimens. During the tests, the critical fracture load P_{c} was determined by SEM images and load-displacement curves, as shown in

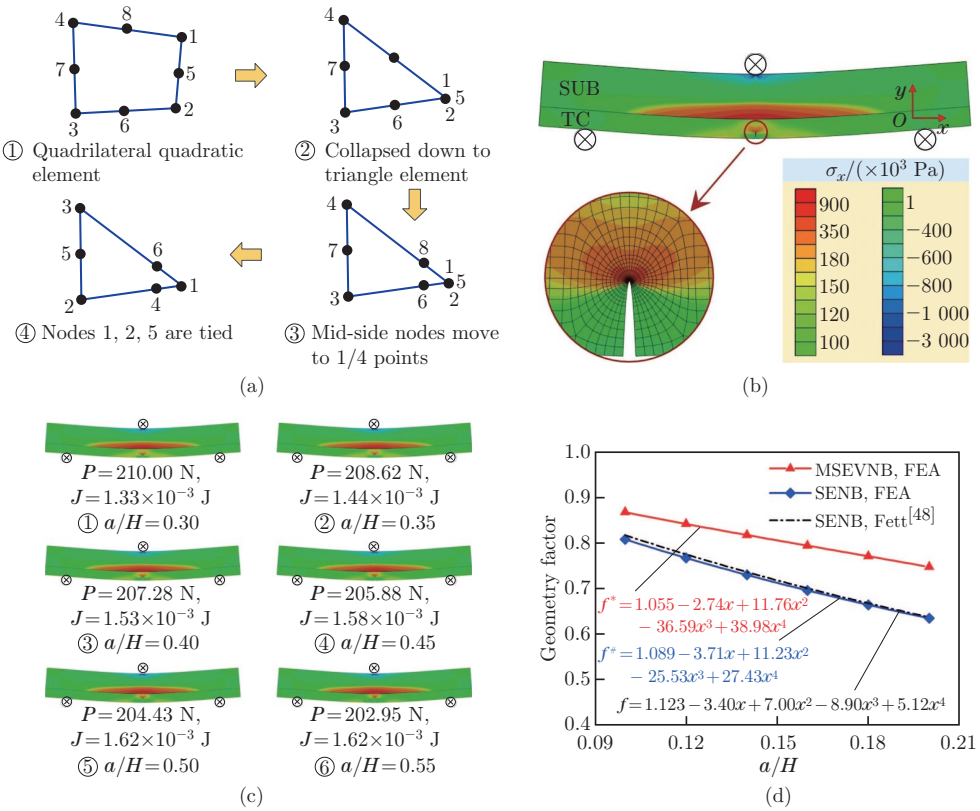

Fig. 5 Determination of the geometry factor of APS TBCs by the FEA: (a) formation of collapse elements, (b) model geometry and stress distribution around the crack tip where SUB represents substrate and TC represents top coat, (c) results of contour integral at different a/H, and (d) geometry factors as a function of a/H (color online)

Fig. 6. It can be seen that the load-displacement curves of the MSEVNB and SENB specimens are straight lines after crack initiation in the top coat (see Figs. 6(a) and 6(b)). It is because the height and elastic modulus of the substrate are larger than those of the top coat, and the substrate is still in linear elastic segment when cracks extend in top coat during the 3PB tests. As a result, the load-displacement curves mainly present the linear mechanical behavior of the substrate. Then, the critical fracture loads P_c of the MSEVNB and SENB specimens are determined as (44.13 ± 3.60) N and (80.54 ± 6.80) N, respectively. According to Eqs. (9) and (12), the corresponding critical fracture stress σ_c^{VN} of the MSEVNB specimens is determined as (34.46 ± 2.10) MPa, while the corresponding critical fracture stress σ_c^{N} of the SENB specimens is determined as (55.34 ± 3.83) MPa. As a result, the critical fracture stress could be overestimated by 60.59% when using the SENB specimens with the notch root radius of 50 μm to replace the MSEVNB specimens with the notch root radius of 10 μm.

3.2.3 Porosity calibration coefficient induced by porosity

Unlike dense materials, the top coat material is porous. Therefore, the effects of porosity on the fracture toughness measurement should also be considered. For bulk materials, Jelitto and Schneider[44] have developed the equation of fracture toughness between porous materials and dense materials. However, Jelitto's model must obtain the fracture strength of dense material, which could not be measured in APS TBCs. It is because TBCs with the dense top coat could not be manufactured by APS technology. Hence, a new calibration model of porosity in APS TBCs should be established.

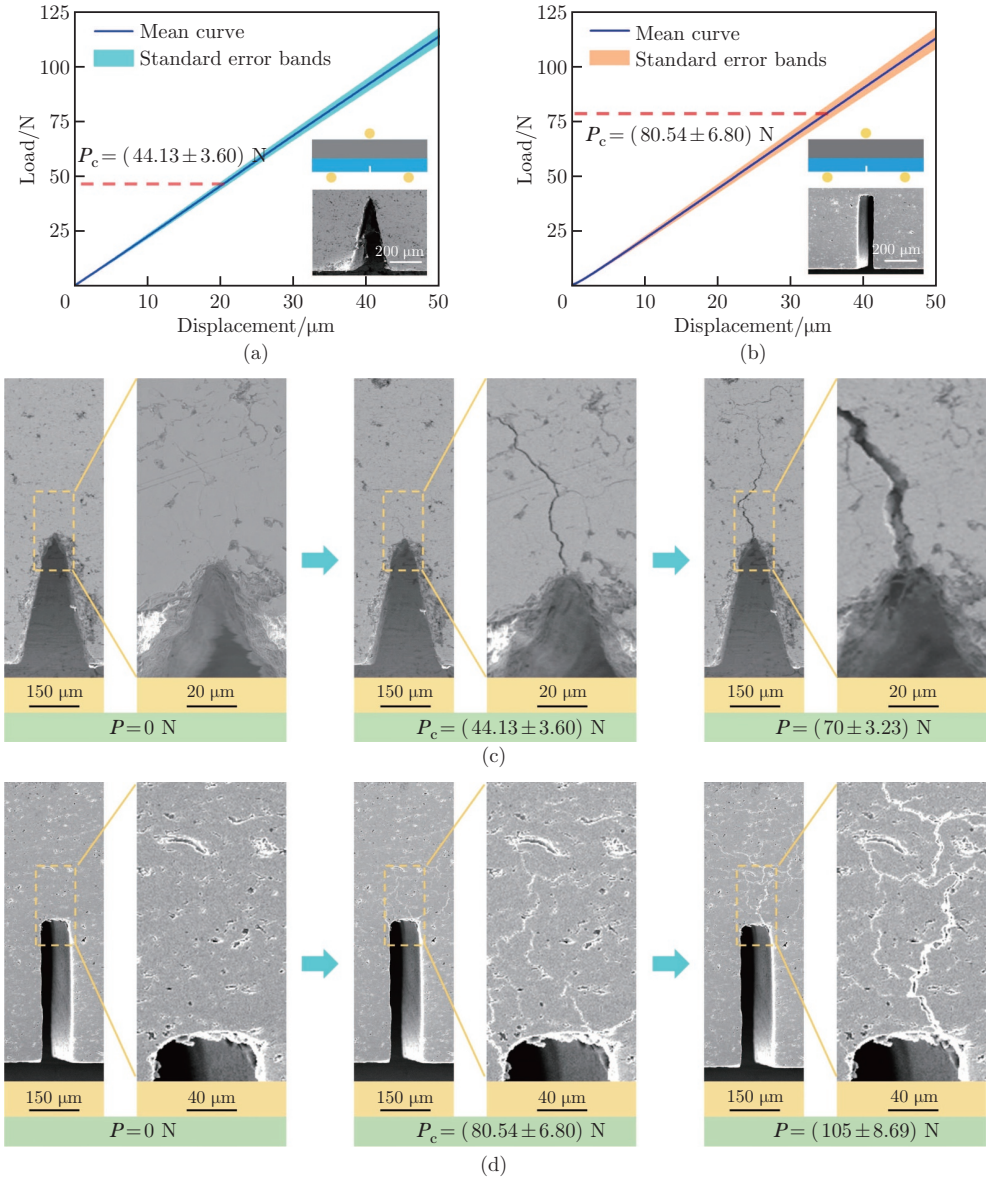

Fig. 6 Typical load-displacement curves of (a) the MSEVNB specimens and (b) the SENB specimens and fracture processes at the notch tips of (c) the MSEVNB specimens and (d) the SENB specimens (color online)

In view of Irwin and Dewit[34], the critical stress intensity factor K_{Ic} represents the stress distribution at the crack tip when the crack is initiated in dense materials. Therefore, it is difficult to express the K_{Ic} influenced by the irregular defects in a porous material. However, the following critical energy release rate G_{Ic} is a more suitable parameter to express the fracture toughness in porous materials[44]:

$$G_{Ic} = \frac{dW}{dA}, \tag{13}$$

where W is the work required to create new fracture surfaces with the area A. The fracture toughness influenced by defects could be switched to the area reduction of fracture surfaces.

Above that, K_{Ic} could be transformed into G_{Ic} based on the LEFM by

$$G_{\mathrm{Ic}} = \frac{1-\nu}{E} K_{\mathrm{Ic}}^2. \tag{14}$$

Then, a porosity calibration equivalent coefficient is proposed, and the critical stress intensity factor of porous materials K_{Ic}^* is expressed as (a detailed derivation of the porosity calibration coefficient $1/\sqrt{1-\varphi}$ is given in Appendix C)

$$K_{\mathrm{Ic}}^* = \frac{1}{\sqrt{1-\varphi}} K_{\mathrm{Ic}}, \tag{15}$$

where φ is the porosity of the top coat.

To quantitatively characterize the porosity, 500 2D image slices of the top coat are acquired by X-CT. Three-dimensional (3D) volume rendering of the top coat is obtained by stacking 2D images, as shown in Fig. 7(a). A greyscale-based interactive threshold segmentation method is used to extract the 3D morphology of defects in the top coat, as shown in Fig. 7(b). Then, the porosity of the top coat is counted as 19.57%. Based on Eq. (15), the corresponding porosity calibration coefficient is determined as 1.115 0. Without considering the influence induced by micro-defects, the surface fracture toughness may be overestimated by 13.1%, compared with that taking the effects of micro defects into consideration.

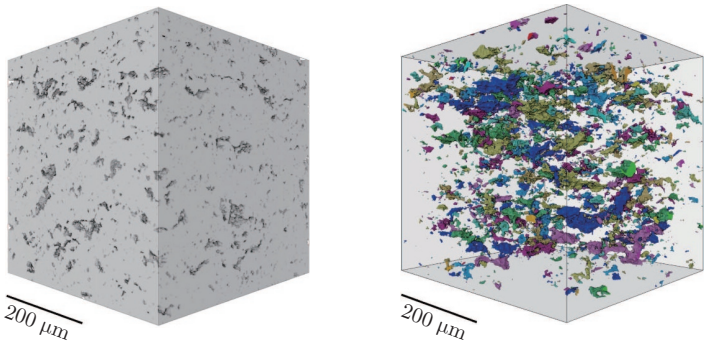

Fig. 7 (a) 3D volume rendering of the top coat and (b) 3D morphology of defect distribution in the top coat (color online)

3.2.4 Surface fracture toughness measured by MSEVNB method

Considering the multilayer and porous characters, the MSEVNB method is used to measure the fracture toughness of APS TBCs. Based on the above analysis, the expression of the MSEVNB method can be written as

$$K_{\mathrm{Ic}}^{\mathrm{VN}} = \frac{1}{\sqrt{1-\varphi}} f^* \sigma_{\mathrm{c}}^{\mathrm{VN}} \sqrt{\pi a}. \tag{16}$$

The expression of the SENB method is written as

$$K_{\mathrm{Ic}}^{\mathrm{N}} = f \sigma_{\mathrm{c}}^{\mathrm{N}} \sqrt{\pi a}. \tag{17}$$

The specimens of the experimental group and control group are tested by the in-situ SEM. Based on Eq. (16), the surface fracture toughness of the MSEVNB specimens in the experimental group is determined as (1.12 ± 0.06) MPa. One of the SENB specimens in the control group is determined as (1.79 ± 0.12) MPa. Those results are plotted in Fig. 8. It is clear that the surface fracture toughness measured by the SENB method without considering the characters of APS TBCs is 59.82% larger than that measured by the MSEVNB method.

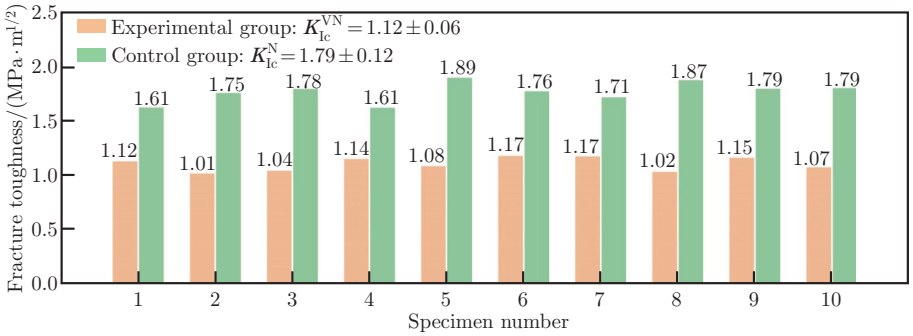

Fig. 8 Surface fracture toughness measured by the MSEVNB and SENB methods (color online)

3.2.5 Accuracy of MSEVNB method

To verify the accuracy of the MSEVNB method, another type of MSEVNB specimens is prepared. The freestanding MSEVNB specimens are obtained by dissolving the substrate and bond coat of beam specimens and set as the verification group-1. The typical load-displacement curve and the fracture process at the notch tip are shown in Figs. 9(a) and 9(b).

Without multilayer structures, the residual stress in the top coat is absent, and the geometry factor f with $S/H=8$ could be provided by[48]

$$f(x)=1.094-1.91x+3.20x^2-2.64x^3+0.74x^4. \tag{18}$$

The critical fracture stress σ_c is determined as (51.38 ± 0.53) MPa, and is calculated by

$$\sigma_c^{VN}=\frac{3P_cS}{2B(h_{TC}-a)^2}. \tag{19}$$

The surface fracture toughness of freestanding MSEVNB specimens is determined as (1.20 ± 0.12) MPa·m$^{1/2}$ and plotted in Fig. 9(c), which is close to that of the MSEVNB specimens in the experimental group. Thus, the surface fracture toughness obtained by the MSEVNB method is valid.

3.3 General validation of MSEVNB methods

3.3.1 Independence of top coat thickness

To verify the independence of the top coat thickness on the surface fracture toughness measured by the MSEVNB method, the verification group-2 and the verification group-3 are set. Except for the top coat thickness, the specimens of these two new groups are the same as those in the experimental group. The residual stresses in the top coat corresponding to different specimens are also measured, as shown in Fig. 10(a). The geometry factors of different groups are determined by the FEA, as shown in Fig. 10(b). Typical load-displacement curves in the verification group-2 and the verification group-3 are plotted in Figs. 10(c) and 10(d), respectively. Finally, the surface fracture toughnesses of these two groups are evaluated and plotted in Fig. 10(e). The surface fracture toughnesses are determined as (1.11 ± 0.06) MPa·m$^{1/2}$ and (1.07 ± 0.07) MPa·m$^{1/2}$ for the verification group-2 and the verification group-3, respectively. These values are close to (1.12 ± 0.06) MPa·m$^{1/2}$, which is obtained from the experimental group. Thus, the surface fracture toughness measured by the MSEVNB method is independent of the top coat thickness.

3.3.2 Independence of specimen width

To obtain the reliable surface fracture toughness, the independence of specimen width on the surface fracture toughness measured by the MSEVNB method is also studied. The experimental model proposed by Fisher abd Barsom[50] explains a possible variation of the measured fracture toughness with specimen width. The measured values decrease with increasing the

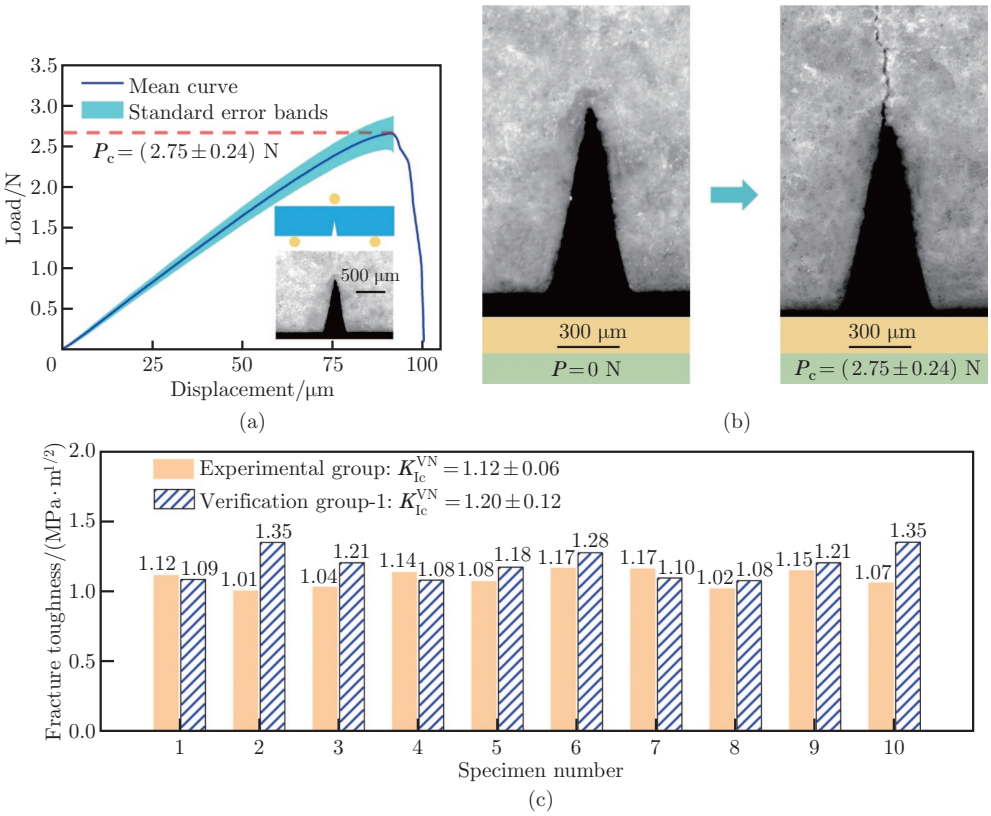

Fig. 9 Results of the verification group-1: (a) typical load-displacement curve, (b) fracture process at the notch tip, and (c) surface fracture toughness (color online)

specimen width until a plateau is reached. In that plateau, the toughness appears to be relatively insensitive to the specimen width, and is referred to as "plane strain fracture toughness". The specimen width obeys the following relationship:

$$B \geqslant B_0 = 2.5\left(\frac{K_{\mathrm{Ic}}}{\sigma_{\mathrm{ys}}}\right)^2, \tag{20}$$

where σ_{ys} is the yield stress of the top coat, and B_0 is the critical specimen width. It is well-known that the mechanical behavior of brittle materials does not exhibit yielding[51]. The ultimate strength σ_{b} is generally used in place of yield strength σ_{ys} in brittle materials. The ultimate strength σ_{b} of the top coat is defined as the stress corresponding to the crack initiation in the top coat. Similar to the derivation of the critical fracture stress σ_{c}, the ultimate strength σ_{b} is expressed as

$$\sigma_{\mathrm{b}} = \frac{12E_{\mathrm{TC}}P_{\mathrm{b}}Sh_1}{E_{\mathrm{SUB}}B((h_1-h_{\mathrm{TC}})^3-(h_1-H)^3)+E_{\mathrm{TC}}B(h_1^3-(h_1-h_{\mathrm{TC}})^3)} + \sigma_{\mathrm{res}}^{\mathrm{top}}, \tag{21}$$

where P_{b} is the critical break load corresponding to the crack initiation in the top coat. $\sigma_{\mathrm{res}}^{\mathrm{top}}$ is the residual stress on the surface of the top coat.

In-situ 3PB tests are conducted on the beam specimens in the basic group. The typical load-displacement curve and SEM images at the critical break load are shown in Figs. 11(a) and 11(b), respectively. P_{b} is determined as (119.45 ± 9.75) N. $\sigma_{\mathrm{res}}^{\mathrm{top}}$ is (19 ± 2.3) MPa, which has been discussed in Fig. 5. According to Eq. (21), the ultimate strength σ_{b} is determined

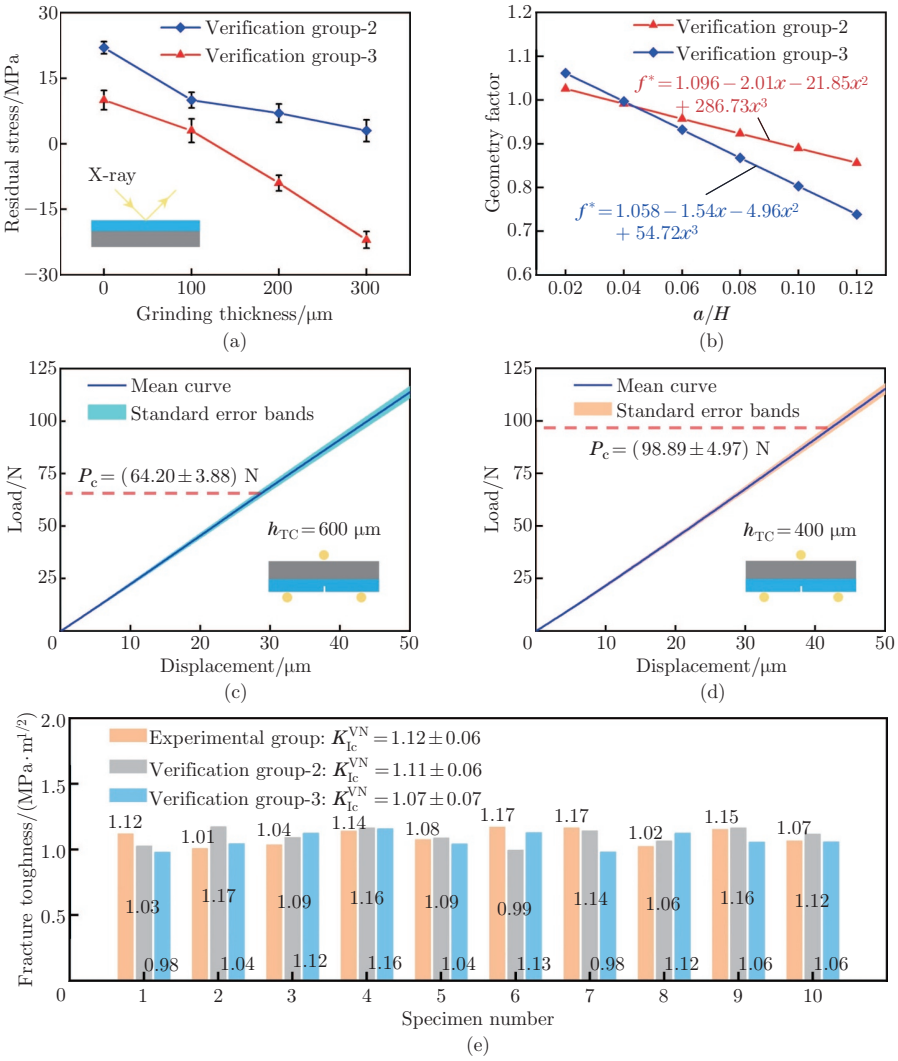

Fig. 10 (a) Residual stresses in the top coat, (b) geometry factors, typical load-displacement curves of (c) the verification group-2 and (d) the verification group-3, and (e) surface fracture toughness (color online)

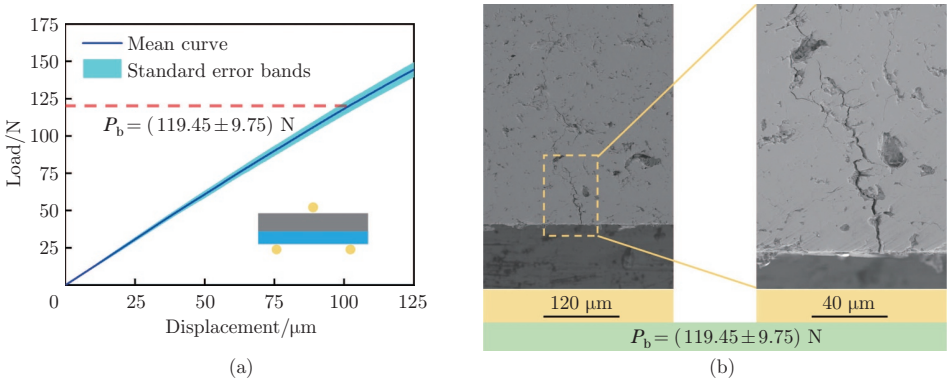

Fig. 11 (a) Typical load-displacement curve and (b) SEM images at the critical break load (color online)

as (84.72 ± 5.03) MPa. Combining the surface fracture toughness measured by the MSEVNB method, B_0 is calculated as 0.5 μm, which is less than the specimen width (2 mm and 0.9 mm in this study). Thus, the surface fracture toughness measured by the MSEVNB method is independent of the specimen width.

4 Conclusions

In this work, the MSEVNB method is developed to evaluate the surface fracture toughness of APS TBCs. The typical structural characters of APS TBCs are taken into account. The effects of multilayer and porous characters on the measured surface fracture toughness are studied quantitatively. The main conclusions are summarized as follows.

(i) Considering the multilayer structure of APS TBCs, the geometry factor f^* is recalculated through the FEA, and is 9.9% higher than f, which ignores the multilayer structure.

(ii) The critical fracture stress of the MSEVNB specimens with the notch root radius of 10 μm is 37.7% lower than that obtained from the SENB specimens with the notch root radius of 50 μm.

(iii) Considering the reduction area of the crack surface induced by micro-defects, a calibration coefficient of porosity is proposed. The surface fracture toughness measured after porosity calibration is 11.5% higher than that obtained from the SENB method.

(iv) The surface fracture toughness of APS TBCs measured by the MSEVNB method is determined as (1.12 ± 0.06) MPa, which is 37.4% lower than that measured by the SENB method.

(v) It is found that the surface fracture toughness measured by the MSEVNB method is independent of the top coat thickness and specimen width.

References

[1] CHEN, L. B. Yttria-stabilized zirconia thermal barrier coatings — a review. *Surface Review and Letters*, **13**(5), 535–544 (2006)

[2] MONDAL, K., NUNEZ, L., DOWNEY, C. M., and VAN ROOYEN, I. J. Thermal barrier coatings overview: design, manufacturing, and applications in high-temperature industries. *Industrial & Engineering Chemistry Research*, **60**(17), 6061–6077 (2021)

[3] MEHBOOB, G., LIU, M. J., XU, T., HUSSAIN, S., MEHBOOB, G., and TAHIR, A. A review on failure mechanism of thermal barrier coatings and strategies to extend their lifetime. *Ceramics International*, **46**(7), 8497–8521 (2020)

[4] LI, C. J., LI, Y., YANG, G. J., and LI, C. X. Evolution of lamellar interface cracks during isothermal cyclic test of plasma-sprayed 8YSZ coating with a columnar-structured YSZ interlayer. *Journal of Thermal Spray Technology*, **22**(8), 1374–1382 (2013)

[5] JIANG, J., WU, D., WANG, W., ZHAO, X., MA, X., WANG, B., and SHI, H. J. Fracture behavior of TBCs with cooling hole structure under cyclic thermal loadings. *Ceramics International*, **46**(3), 3644–3654 (2020)

[6] WEI, Z. Y., CAI, H. N., and ZHAO, S. D. Study on spalling mechanism of APS thermal barrier coatings considering surface vertical crack evolution affected by surrounding cracks. *Ceramics International*, **48**(8), 11445–11455 (2022)

[7] KOKINI, K., CHOULES, B. D., and TAKEUCHI, Y. R. Thermal fracture mechanisms in ceramic thermal barrier coatings. *Journal of Thermal Spray Technology*, **6**(1), 43–49 (1997)

[8] HILLE, T. S., SUIKER, A. S. J., and TURTELTAUB, S. Microcrack nucleation in thermal barrier coating systems. *Engineering Fracture Mechanics*, **76**(6), 813–825 (2009)

[9] RUBINSTEIN, A. A. and TANG, Y. Analysis of crack nets development in thermal barrier coatings. *International Journal of Fracture*, **151**(1), 57–79 (2008)

[10] SONG, D., SONG, T., PAIK, U., LYU, G., JUNG, Y. G., CHOI, B. G., KIM, I. S., and ZHANG, J. Crack-growth behavior in thermal barrier coatings with cyclic thermal exposure. *Coatings*, **9**(6), 365 (2019)

[11] MILLER, R. A. Oxidation-based model for thermal barrier coating life. *Journal of the American Ceramic Society*, **67**(8), 517–521 (1984)

[12] TAKAHASHI, S., YOSHIBA, M., and HARADA, Y. Microstructural features of mechanical failure in thermal barrier coating systems under static loadings. *Materials at High Temperatures*, **18**(2), 125–130 (2001)

[13] EVANS, A. G., MUMM, D. R., HUTCHINSON, J. W., MEIER, G. H., and PETTIT, F. S. Mechanisms controlling the durability of thermal barrier coatings. *Progress in Materials Science*, **46**(5), 505–553 (2001)

[14] HE, M. Y., MUMM, D. R., and EVANS, A. G. Criteria for the delamination of thermal barrier coatings: with application to thermal gradients. *Surface and Coatings Technology*, **185**(2), 184–193 (2004)

[15] HUTCHINSON, J. W. and SUO, Z. Mixed mode cracking in layered materials. *Advances in Applied Mechanics*, **29**, 63–191 (1991)

[16] THOMPSON, J. A. and CLYNE, T. W. The effect of heat treatment on the stiffness of zirconia top coats in plasma-sprayed TBCs. *Acta Materialia*, **49**(9), 1565–1575 (2001)

[17] ZHANG, S., SUN, D., FU, Y., and DU, H. Toughness measurement of thin films: a critical review. *Surface and Coatings Technology*, **198**(1), 74–84 (2005)

[18] MAO, W. G., CHEN, Y. Y., WANG, Y. J., ZHOU, M., YANG, H. Y., WANG, Z., DAI, C. Y., CHEN, X., and FANG, D. N. A multilayer structure shear lag model applied in the tensile fracture characteristics of supersonic plasma sprayed thermal barrier coating systems based on digital image correlation. *Surface and Coatings Technology*, **350**, 211–226 (2018)

[19] YAO, W. B., DAI, C. Y., MAO, W. G., LU, C., YANG, L., and ZHOU, Y. C. Acoustic emission analysis on tensile failure of air plasma-sprayed thermal barrier coatings. *Surface and Coatings Technology*, **206**(18), 3803–3807 (2012)

[20] YANG, L., ZHONG, Z. C., ZHOU, Y. C., and LU, C. S. Quantitative assessment of the surface crack density in thermal barrier coatings. *Acta Mechanica Sinica*, **30**(2), 167–174 (2014)

[21] YANG, L., ZHONG, Z. C., YOU, J., ZHANG, Q. M., ZHOU, Y. C., and TANG, W. Z. Acoustic emission evaluation of fracture characteristics in thermal barrier coatings under bending. *Surface and Coatings Technology*, **232**, 710–718 (2013)

[22] JIANG, P., FAN, X., SUN, Y., LI, D., and WANG, T. Bending-driven failure mechanism and modelling of double-ceramic-layer thermal barrier coating system. *International Journal of Solids and Structures*, **130-131**, 11–20 (2018)

[23] ZHANG, X., WATANABE, M., and KURODA, S. Effects of residual stress on the mechanical properties of plasma-sprayed thermal barrier coatings. *Engineering Fracture Mechanics*, **110**, 314–327 (2013)

[24] LIU, H., LIANG, L., WANG, Y., and WEI, Y. Fracture characteristics and damage evolution of coating systems under four-point bending. *International Journal of Applied Ceramic Technology*, **13**(6), 1043–1052 (2016)

[25] MALZBENDER, J. and STEINBRECH, R. W. Fracture resistance of atmospheric plasma sprayed thermal barrier coatings. *Surface and Coatings Technology*, **209**, 97–102 (2012)

[26] THURN, G., SCHNEIDER, G. A., BAHR, H. A., and ALDINGER, F. Toughness anisotropy and damage behavior of plasma sprayed ZrO_2 thermal barrier coatings. *Surface and Coatings Technology*, **123**(2), 147–158 (2000)

[27] ANG, A. S. M. and BERNDT, C. C. A review of testing methods for thermal spray coatings. *International Materials Reviews*, **59**(4), 179–223 (2014)

[28] SEBASTIANI, M., JOHANNS, K. E., HERBERT, E. G., and PHARR, G. M. Measurement of fracture toughness by nanoindentation methods: recent advances and future challenges. *Current Opinion in Solid State and Materials Science*, **19**(6), 324–333 (2015)

[29] EBERL, C., GIANOLA, D. S., and HEMKER, K. J. Mechanical characterization of coatings using microbeam bending and digital image correlation techniques. *Experimental Mechanics*, **50**(1), 85–97 (2010)

[30] LI, C. J., WANG, W. Z., and HE, Y. Dependency of fracture, toughness of plasma sprayed Al_2O_3 coatings on lamellar structure. *Journal of Thermal Spray Technology*, **13**(3), 425–431 (2004)

[31] OSTOJIC, P. and MCPHERSON, R. Determining the critical strain-energy release rate of plasma-sprayed coatings using a double-cantilever-beam technique. *Journal of the American Ceramic Society*, **71**(10), 891–899 (1988)

[32] YANG, X. S., WAN, J., DAI, C. Y., ZHANG, Y., MAO, W. G., ZHOU, Y. C., and LU, C. Finite element analysis of crack propagation and fracture mechanical properties of freestanding 8wt.% Y_2O_3-ZrO_2 coatings. *Surface and Coatings Technology*, **223**, 87–91 (2013)

[33] ZHU, W., WU, Q., YANG, L., and ZHOU, Y. C. In situ characterization of high temperature elastic modulus and fracture toughness in air plasma sprayed thermal barrier coatings under bending by using digital image correlation. *Ceramics International*, **46**, 18526–18533 (2020)

[34] IRWIN, G. and DEWIT, R. A summary of fracture-mechanics concepts. *Journal of Testing and Evaluation*, **11**(1), 56–65 (1983)

[35] QUINN, G. D. and BRADT, R. C. On the Vickers indentation fracture toughness test. *Journal of the American Ceramic Society*, **90**(3), 673–680 (2007)

[36] JUNGK, J., BOYCE, B., BUCHHEIT, T., FRIEDMANN, T., YANG, D., and GERBERICH, W. Indentation fracture toughness and acoustic energy release in tetrahedral amorphous carbon diamond-like thin films. *Acta Materialia*, **54**(15), 4043–4052 (2006)

[37] JEON, S. W., LEE, K. W., KIM, J. Y., KIM, W. J., PARK, C. P., and KWON, D. Estimation of fracture toughness of metallic materials using instrumented indentation: critical indentation stress and strain model. *Experimental Mechanics*, **57**(7), 1013–1025 (2017)

[38] IQBAL, F., AST, J., GOKEN, M., and DURST, K. In situ micro-cantilever tests to study fracture properties of NiAl single crystals. *Acta Materialia*, **60**(3), 1193–1200 (2012)

[39] MORRELL, R. Fracture toughness testing for advanced technical ceramics: internationally agreed good practice. *Advances in Applied Ceramics*, **105**(2), 88–98 (2006)

[40] GOGOTSI, G. A. Fracture toughness of ceramics and ceramic composites. *Ceramics International*, **29**(7), 777–784 (2003)

[41] GOGOTSI, G., MUDRIK, S., and GALENKO, V. Evaluation of fracture resistance of ceramics: edge fracture tests. *Ceramics International*, **33**(3), 315–320 (2007)

[42] FORSCHELEN, P. J. J., SUIKER, A. S. J., and VAN DER SLUIS, O. Effect of residual stress on the delamination response of film-substrate systems under bending. *International Journal of Solids and Structures*, **97-98**, 284–299 (2016)

[43] TEIXEIRA, V., RITSCHKY, M., FISCHER, W., BUCHKREMER, H. P., and STOVER, D. Analysis of residual stresses in thermal barrier coatings. *Journal of Materials Processing Technology*, **93**, 209–216 (1999)

[44] JELITTO, H. and SCHNEIDER, G. A. A geometric model for the fracture toughness of porous materials. *Acta Materialia*, **151**, 443–453 (2018)

[45] CHIU, C. C. and CASE, E. D. Elastic modulus determination of coating layers as applied to layered ceramic composites. *Materials Science and Engineering*: *A*, **132**, 39–47 (1991)

[46] WANG, X., TINT, S., CHIU, M., and ATKINSON, A. Stiffness of free-standing thermal barrier coating top coats measured by bending tests. *Acta Materialia*, **60**(8), 3247–3258 (2012)

[47] ZHU, L., XU, B., WANG, H., and WANG, C. On the evaluation of residual stress and mechanical properties of FeCrBSi coatings by nanoindentation. *Materials Science and Engineering*: *A*, **536**, 98–102 (2012)

[48] FETT, T. An analysis of the three-point bending bar by use of the weight function method. *Engineering Fracture Mechanics*, **40**(3), 683–686 (1991)

[49] WANG, Y. B. Boundary element analysis of interaction between an elastic rectangular inclusion and a crack. *Applied Mathematics and Mechanics* (*English Edition*), **25**(2), 152–157 (2004) https://doi.org/10.1007/BF02437316

[50] FISHER, J. W. and BARSOM, J. M. Evaluation of cracking in the rib-to-deck welds of the bronx-whitestone bridge. *Journal of Bridge Engineering*, **21**(3), 04015065 (2016)

[51] XU, Y., AN, B., ZHANG, D., and WANG, R. Region dependent fracture resistance behavior of human dentin based on numerical simulation. *Applied Mathematics and Mechanics* (*English Edition*), **35**(3), 277–284 (2014) https://doi.org/10.1007/s10483-014-1790-8

Appendix A Detailed interpretation of the geometry factor f

According to Fett[48], the critical stress intensity factor of the SENB method (see Fig. A1(a)) in the 3PB tests could be expressed as

$$K_{\mathrm{Ic}} = f_1\sigma_0\sqrt{\pi a} = f_2\sigma_{\mathrm{c}}\sqrt{\pi a}, \tag{A1}$$

where σ_0 is the characteristic stress and can be expressed as

$$\sigma_0 = \frac{3P_{\mathrm{c}}S}{2BH^2}, \tag{A2}$$

while σ_{c} is the critical fracture stress and can be expressed as

$$\sigma_{\mathrm{c}} = \frac{3P_{\mathrm{c}}S}{2B(H-a)^2}. \tag{A3}$$

Combining Eqs. (A1)–(A3), the geometry factor f_1 corresponding to the characteristic stress can be switched to the geometry factor f_2 corresponding to the critical fracture stress through

$$f_2 = \left(1-\frac{a}{H}\right)^2 f_1. \tag{A4}$$

Those two forms of the geometry factor are plotted in Fig. A1(b). It is obvious that f_1 increases while f_2 decreases when a/H increases. In this paper, the form of f_2 is chosen. It is because the corresponding critical fracture stress is easy to define in the TBCs with the multilayer structure.

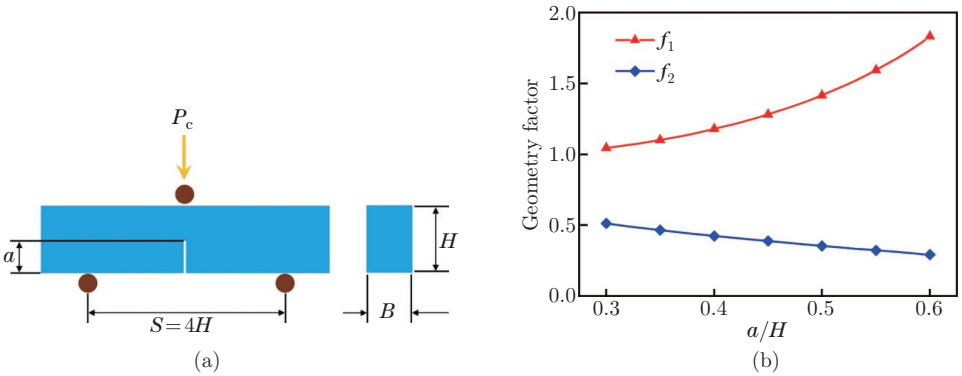

Fig. A1 (a) Schematic of the SENB method; (b) geometry factors of two forms (color online)

Appendix B Derivation of the critical fracture stress

During 3PB tests, the notched specimen can be regarded as a double-layer composite beam with the top coat thickness of $(h_{\mathrm{TC}}-a)$.

The moment of the notched specimens induced by the critical load P_{c} can be expressed as

$$M = \frac{P_{\mathrm{c}}S}{4}. \tag{B1}$$

The moments of the substrate M_{SUB} and the top coat M_{TC} follow the superposition principle as follows:

$$M = M_{\mathrm{TC}} + M_{\mathrm{SUB}}. \tag{B2}$$

The curvature radius of the neutral axis ρ in the notched specimens can be expressed as

$$\frac{1}{\rho} = \frac{M_{\mathrm{SUB}}}{E_{\mathrm{SUB}} I_{\mathrm{SUB}}}, \quad \frac{1}{\rho} = \frac{M_{\mathrm{TC}}}{E_{\mathrm{TC}} I_{\mathrm{TC}}}, \tag{B3}$$

where I_{TC} is the moment inertia of the top coat to the neutral axis for the notched specimens, and the moment inertia for the substrate I_{SUB} is expressed as

$$I_{\mathrm{SUB}} = B \int_{h_2 - H}^{h_2 - h_{\mathrm{TC}}} y^2 \mathrm{d}y, \quad I_{\mathrm{TC}} = B \int_{h_2 - h_{\mathrm{TC}}}^{h_2 - a} y^2 \mathrm{d}y. \tag{B4}$$

The bending stress σ_{TC} of the top coat is given by

$$\sigma_{\mathrm{TC}} = \frac{M_{\mathrm{TC}}}{I_{\mathrm{TC}}} y. \tag{B5}$$

The critical fracture stress of the top coat σ_{c} can be determined through

$$\sigma_{\mathrm{c}} = \sigma_{\mathrm{TC}}\big|_{y = h_2 - a}. \tag{B6}$$

Combining Eqs. (B1)–(B6), the critical fracture stress of the top coat σ_{c} can be indicated as

$$\sigma_{\mathrm{c}} = \frac{12 E_{\mathrm{TC}} P_{\mathrm{c}} S (h_2 - a)}{E_{\mathrm{SUB}} B((h_2 - h_{\mathrm{TC}})^3 - (h_2 - H)^3) + E_{\mathrm{TC}} B((h_2 - a)^3 - (h_2 - h_{\mathrm{TC}})^3)}. \tag{B7}$$

Similar to h_1 expressed by Eq. (4)[46], the distance h_2 from the neutral axis to the surface of the top coat in the notched specimen can be determined by

$$h_2 = \frac{E_{\mathrm{SUB}} h_{\mathrm{SUB}}^2 - E_{\mathrm{TC}} (h_{\mathrm{TC}} - a)^2}{2 E_{\mathrm{SUB}} h_{\mathrm{SUB}} + 2 E_{\mathrm{TC}} (h_{\mathrm{TC}} - a)} + h_{\mathrm{TC}}. \tag{B8}$$

Appendix C Derivation of the porosity calibration coefficient

The critical energy release rate G_{Ic} is usually used to characterize the fracture behavior of porous material. G_{Ic} describes the energy balance when cracks extend in materials[52]. In dense materials, G_{Ic} can be expressed as

$$G_{\mathrm{Ic}} = \frac{\mathrm{d}W}{\mathrm{d}A}, \tag{C1}$$

where W is the work required to create new fracture surfaces with the area of A. It is worth noting that micro-defects in porous materials may reduce the area of the fracture surfaces. The effects of micro-defects on the area of fracture surfaces should be considered. Given the porosity φ, the real area of fracture surfaces in the porous material A^* can be written as

$$\frac{A^*}{A} = 1 - \varphi. \tag{C2}$$

Accordingly, the critical energy release rate of the porous materials G_{Ic}^* can be calibrated as

$$G_{\mathrm{Ic}}^* = \frac{\mathrm{d}W}{\mathrm{d}A^*} = \frac{1}{1 - \varphi} G_{\mathrm{Ic}}. \tag{C3}$$

Based on the LEFM, the relationship between G_{Ic} and K_{Ic} in dense materials could be expressed as

$$G_{\mathrm{Ic}} = \frac{1 - \nu}{E} K_{\mathrm{Ic}}^2. \tag{C4}$$

A similar relationship exists in porous materials, and can be written as

$$G_{\mathrm{Ic}}^* = \frac{1 - \nu}{E} K_{\mathrm{Ic}}^{*2}, \tag{C5}$$

where K_{Ic}^* is the critical stress intensity factor of the porous materials. Combining Eqs. (C3)–(C5), K_{Ic}^* can be rewritten as

$$K_{\mathrm{Ic}}^* = \frac{1}{\sqrt{1 - \varphi}} K_{\mathrm{Ic}}. \tag{C6}$$